EXPERIMENTAL INVESTIGATION OF TRANSIENT FLOW PHENOMENA IN ROTATING COMPRESSOR CAVITIES

Mikolaj J. Pernak[1], Tom E. W. Nicholas[1], Jake T. Williams[2], Richard W. Jackson[1], Hui Tang[1], Gary D. Lock[1], James A. Scobie[1,*]

[1]Department of Mechanical Engineering, University of Bath, Bath BA2 7AY, United Kingdom
[2]Rolls-Royce plc, Filton, Bristol BS34 7QE, United Kingdom

mjp210@bath.ac.uk, tewn20@bath.ac.uk, Jake.Williams@Rolls-Royce.com, rwj22@bath.ac.uk,
ht377@bath.ac.uk, ensgdl@bath.ac.uk, jas28@bath.ac.uk*

ABSTRACT

The clearance of compressor blade tips during aero-engine accelerations is an important design issue for next-generation engine architectures. The transient clearance depends on the radial expansion of the compressor discs, which is directly coupled to conjugate heat transfer in co-rotating discs governed by unsteady and unstable buoyancy-induced flow. This paper discusses an experimental and modelling study using the Bath Compressor Cavity Rig, which simulates a generic axial compressor at fluid-dynamically scaled conditions. The rig was specifically designed to generate heat transfer of practical interest to the engine designer and validate computational codes. This work presents the first study of the fundamental fluid dynamic and heat transfer phenomena under transient conditions. The rotating flow structure was seen to be characterised by coherent pairs of cyclonic/anti-cyclonic vortex pairs; the strength, rotational frequency, stability and number of these unsteady structures changed with changing rotational Reynolds and Grashof numbers during the transients. These structures, measured by unsteady pressure transducers in the rotating frame of reference, were only present when the flow in the rotating cavity was dominated by buoyancy. Experimental correlations of both Nusselt number and radial mass flow rate in the rotating core were correlated against Grashof number. Remarkably, the experiments revealed a consistent correlation for both steady-state and transient conditions over a wide range of Gr. The results have a practical application to thermo-mechanical models for engine design.

*Corresponding author: jas28@bath.ac.uk

1. INTRODUCTION

The climate crisis necessitates substantial increases in the efficiency of aero-engine technology. Organisational targets to reach net zero emissions require future engine concepts (e.g. open-rotor architectures and embedded engines) with smaller engine cores. Small cores, with even smaller compressor blades, require improved blade-clearance control for efficient operation, especially in transient conditions such as take-off and landing.

The blade clearance depends principally on the temperature distribution of the co-rotating compressor discs to which they are attached. The unsteady buoyancy-induced flow structure inside the rotating cavity creates a strongly conjugate challenge. The temperature distribution across the disc is affected by the temperature and structure of the flow, which in turn is driven by the disc temperature distribution. A fundamental understanding of the flow phenomena is critical to technological advancements.

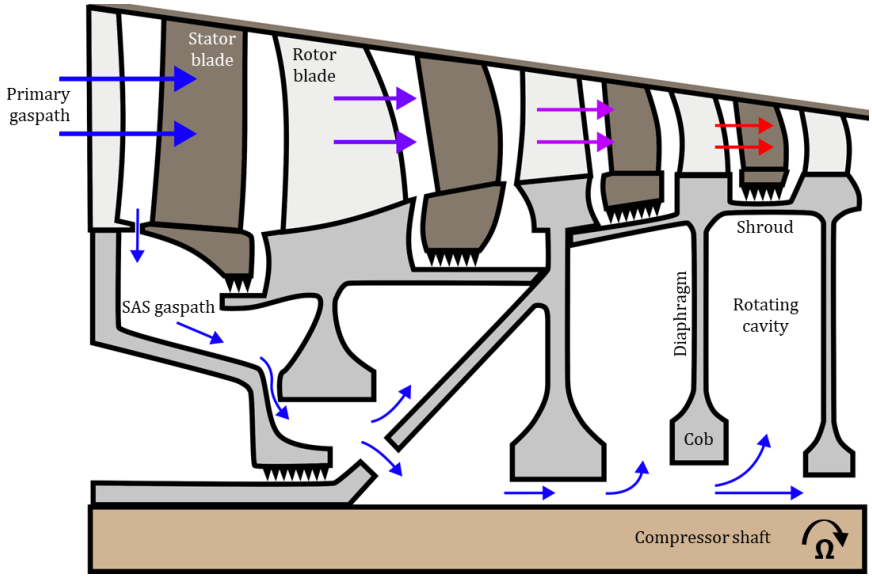

Figure 1: Primary and secondary flow paths through an aero-engine axial compressor. Larger arrows denote primary gas path, smaller arrows denote the Secondary Air System (adapted from [1])

Figure 1 illustrates a conventional axial compressor operating at cruise conditions. Hot mainstream air passes over the compressor blades, and an internal, axial through-flow of secondary flow is used for cooling. Heat is conducted through the shroud and compressor discs and transferred between the primary and secondary flow paths, as well as to the air enclosed in cavities formed between adjacent discs. The temperature gradient in these cavities results in a density gradient, with a flow structure dominated by buoyancy and analogous to Rayleigh-Bénard convection. The fluid dynamics, however, is governed by centrifugal and Coriolis forces rather than gravity. The unsteady flow structure is discussed in Section 2.1, where the circumferential Coriolis forces are created by the pressure distribution from the counter-rotating vortices in the core and shear stresses in the Ekman layers near the discs. Cold air flows radially outward, before bifurcating into a cyclonic and anticyclonic vortex pair, which have low and high pressures respectively. Hot air flows radially inward. The flow structure is disturbed by the axial through-flow at the inner radius and cobs (see Figure 1), with ingestion and mass exchange dependent on the Rossby number. This three-dimensional system is unsteady and unstable, creating a challenge for computational fluid dynamics. At engine conditions, it is unclear whether these flows are laminar or turbulent, chaotic (i.e., aperiodic change in flow structure) or coherent.

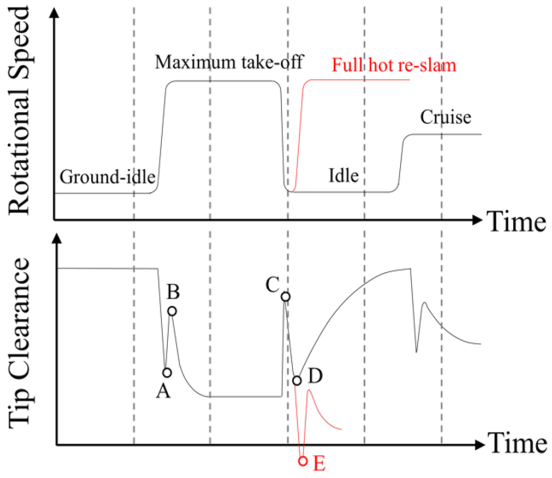

Figure 2: Variation in compressor blade tip clearance across an engine cycle (adapted from [2])

Under transient conditions (e.g. decelerations in the flight cycle) the shroud temperature can decrease rapidly due to the cooling of the mainstream air, and, in some cases, the shroud can be cooler than the throughflow. Here there can be no buoyancy-induced convection and the transition from one regime to the other is yet to be quantified, potentially giving rise to flow instabilities. Flow stability also occurs in some compressor designs that take a mid-stage bleed and flow air forwards, resulting in bores hotter than the mainstream.

The compressor blade tip clearance is driven by two factors: expansion of the discs and expansion of the compressor casing. Since typically the two have different thermal properties and time constants, they change dimensions at different rates during transient operation. Aero-engines are designed to avoid blade rubs, even under extreme conditions, and conservative practice is employed when setting cold-build clearances. The emphasis for future design is on reducing the degree of required margin by further understanding the effect of disc thermal gradients. An example engine test cycle [2] is shown in Figure 2. As the engine rotational speed is increased from idle to take-off setting, the compressor tip clearance is reduced (marked A); there is a brief period of increasing clearance caused by the casing expanding faster than the rotor (marked B). The converse thermal scenario arises during deceleration, as occurs in approach. The closure decreases swiftly (tip clearance increases) with the abrupt reduction in spool speed (C); with a different time constant, the casing cools and contracts at a faster rate than the rotor, creating a local minimum tip clearance (D). Hot re-slam acceleration (see red line) is the term used when the engine is quickly brought to full power during an aborted landing. Here the hot rotor at high rotation speed will expand before it is fully cooled and the compressor clearances will be subjected to a rapid, unpredictable reduction (E); this is considered the worst case in terms of clearance margin.

Calculating and adjusting engine operational clearances is a complex thermo-mechanical design challenge requiring appropriately-validated models. Understanding the transient behaviour of compressors has an impact in terms of supporting the development of industrial design methodology and minimising uncertainty when calibrating against engine test thermal surveys. Success leads to a reduction in the number of engine tests and the amount of instrumentation dedicated to thermal surveys, due to a reduced reliance on engine test data. Ultimately this results in cost savings and increased flexibility in engine test schedules.

This paper uses experiments and modelling to investigate the fundamental fluid dynamics and heat transfer of transient phenomena in rotating compressor cavities. Broadly there are three aspects under both steady-state and transient conditions: disc temperature

measurements, shroud heat transfer correlations, and measurements of the flow structure in the rotating core. The transient information is the first of its kind for compressor cavities.

2. LITERATURE REVIEW

The reader is directed to Owen and Long [3], who reviewed extensively the literature for buoyancy-induced flow related to aero-engine compressors. The shroud heat transfer is usually characterised by the buoyancy parameter $\beta\Delta T$ as well as the Nusselt (Nu), Rossby (Ro), Grashof (Gr) and rotational Reynolds (Re_ϕ) numbers. These are discussed further in Section 4.2. The high-radius flow in the cavity is dominated by rotation, which governs the heat transfer by suppressing radial motion; this flow is disrupted at lower radius by the axial through-flow. At large Ro a toroidal vortex forms in the cavity, creating a destabilising effect, ingestion and significantly influencing the rotating flow structure and heat transfer. At steady-state conditions in aero-engines, Gr is $O(10^{13})$. The flow is dominated by buoyancy, featuring the unsteady large-scale structures discussed in the Introduction. Transient conditions experienced in engine accelerations can produce negative Gr, where the axial through-flow is hotter than the shroud; here the fluid in the cavity can be thermally stratified with reduced heat transfer and consequently changes to compressor-blade clearances.

Buoyancy is also pertinent to industrial gas turbines, where larger cobs (see Figure 1) essentially form a closed compressor cavity. This closed rotating annulus features prominently in the literature as it provides a simplified scenario where the rotating flow in the cavity is isolated. Here the flow structure between the hub (radius a) and shroud (radius b) is similar to the open cavity, though typically there is the formation of multiple vortex pairs (as opposed to a single pair) as illustrated in Figure 3a. Tang and Owen [4] introduced a parameter χ that represents the ratio of temperature rise caused by compressibility effects to temperature differences between cavity shroud and hub. They derived a model for closed cavities directly relating non-dimensional temperatures for the disc and core to three independent non-dimensional governing parameters: Re_ϕ, $\beta\Delta T$, and χ. (Note that $\mathrm{Gr} = \mathrm{Re}_\phi^2\beta\Delta T$ could be used to replace either Re_ϕ or $\beta\Delta T$ as one of the three independent parameters.)

This section reviews recent experimental, CFD and modelling research, focussing on three themes: *flow structure*, *shroud heat transfer correlations*, and *transient experiments*.

2.1 Flow Structure

The flow in rotating cavities is dominated by buoyancy effects created by rotation and the temperature difference between the hot shroud and the cold hub if the cavity is closed, or the cold throughflow if the cavity is open. The flow structure consists of a fluid core separated from the rotor discs by laminar Ekman layers.

For the *closed cavity*, the fluid core is filled with vortical cells similar to Rayleigh-Bénard convection cells. Sun et al. [5] used a compressible code to compute large-scale unsteady vortical flow structures in the closed cavity investigated experimentally by Bohn et al. [6]. King et al. [7] calculated the two-dimensional streamlines in a closed cavity, which showed the existence of multiple pairs of cyclonic and anticyclonic vortices. Owen [8] suggested the flow in a closed cavity tends to organise itself to maximise the rate of entropy production, in turn, maximising heat transfer; this is known as the Maximum Entropy Production principle. It was shown that the number of vortex pairs, n, in the maximum entropy state depends on the geometry of the cavity.

Pitz et al. [9] used a linear stability analysis to study the flow structure in the same cavity used by Sun et al. [5]. Pitz et al. [10]

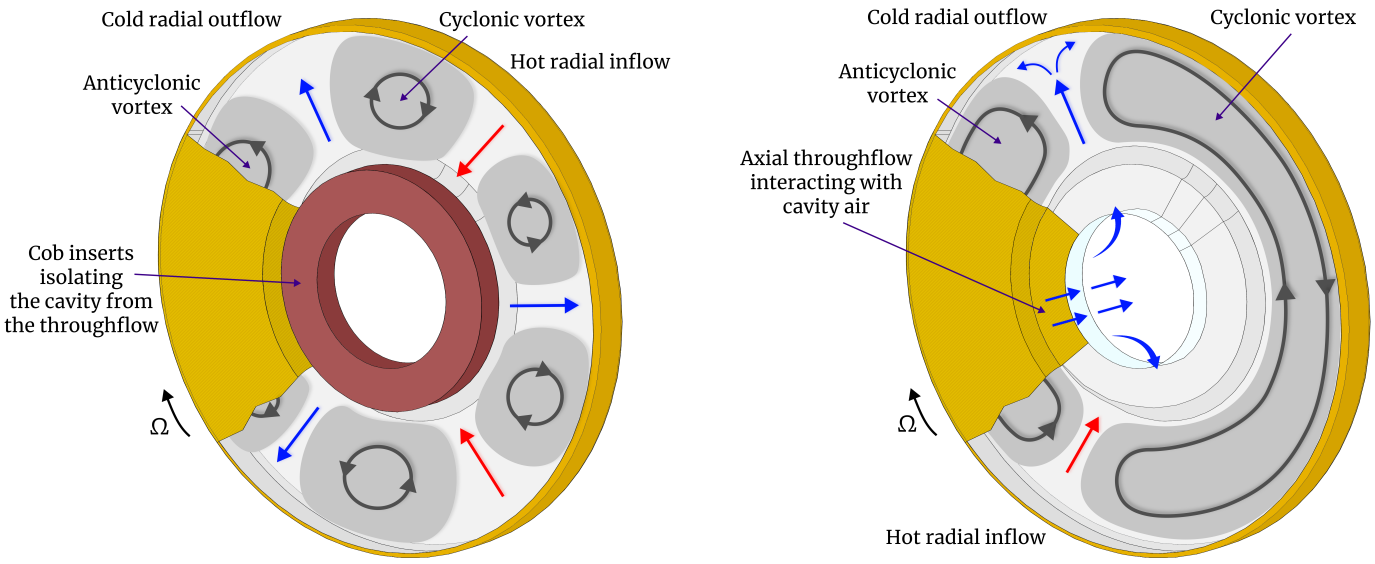

(a) Closed Cavity **(b) Open Cavity**

Figure 3: Flow structure in rotating cavities

also used an incompressible spectral element-Fourier direct numerical simulation (DNS) code with the Boussinesq approximation in the same cavity. The calculated flow structure also consisted of multiple pairs of counter-rotating vortices. The same authors later conducted Large Eddy Simulation (LES) of the flow in the cavity [11]. In addition to the large-scale vortex pairs in the core, laminar Ekman layers were presented using instantaneous velocity profiles. The DNS and LES simulations conducted by Gao et al. [12] further confirmed the laminar behaviour of Ekman layers. Pitz & Wolf [13] used a DNS to investigate the effects of the Coriolis force on buoyancy-driven flows in a cylindrical annulus, noting the stabilising effect of rotation, which was also observed experimentally by Bohn et al. [14, 15] and Jackson et al. [16].

Jackson et al. [16] used high-frequency pressure sensors embedded in rotating discs to measure the flow structure in a closed cavity for the first time. Three or four vortex pairs were detected. The number of vortex pairs increased with increasing Gr, and the structure slipped relative to the discs by less than 1% of the disc speed. Tang and Owen [4] developed theoretical models of the flow in closed rotating cavities. It was suggested that the radial hot and cold plumes between the cyclonic and anticyclonic vortices drive the heat transfer from the hot shroud to the cold hub. The mass flow rates in the plumes are proportional to the circumferential pressure variation created by the vortices, which in turn is determined by the shroud Gr. A correlation between the plume mass flow rate and Gr was established for steady-state cases in Lock et al. [17].

The core in heated *open cavities* is affected by the axial throughflow but is still dominated by buoyancy effects. Smoke visualisation experiments by Farthing et al. [18] showed that under isothermal conditions the extent of throughflow penetration into the cavity is dependent on the Rossby number, Ro. In heated open cavities, a radial cold plume and an asymmetric cyclonic/anticyclonic vortex pair were observed. Tian et al. [19] used an incompressible time-independent code computing Rayleigh-Bénard-like structures appearing in the outer region of the heated cavity. Structures filled the cavity at higher Gr, and the number of vortex pairs and the slip ratio were dependent on Re_ϕ and Gr. The flow visualisation using smoke and a laser light sheet performed by Bohn et al. [20] also showed similar flow behaviour. Long et al. [21] presented Laser Doppler Anemometry measurements of axial, radial and tangential flow velocities in

heated open cavities. The average axial velocity was close to zero, while the average radial velocity was two orders of magnitude lower than the tangential component. The spectral analysis of the tangential velocity showed two pairs of cyclonic and anticyclonic vortices. Jackson et al. [22] investigated the flow structure in an open cavity using unsteady pressure measurements where one cyclonic/anticyclonic vortex pair was revealed across all experimental conditions. The asymmetry of vortex sizes led to a second peak in the analysed frequency spectrum. The slip of the structures varied between 10-15% of the disc speed, dependent on Ro and $\beta\Delta T$ and largely unaffected by Re_ϕ. Gao and Chew [23] used a wall-modelled LES code to simulate the experiments conducted by Jackson et al. [22], showing consistent flow structures and slip ratios. Computational studies conducted by Gao and Chew [24] confirmed laminar Ekman layer behaviour in open cavities.

In summary, typical flow structures in closed and open cavities are illustrated in Figure 3. The number of vortex pairs varies according to the cavity geometry and operating conditions. The dynamic variation of the flow structure in compressor cavities under engine transient operating conditions is investigated here for the first time. For the engine designer, this information creates important scaling laws of the flow and heat transfer in rotating cavities.

2.2 Heat Transfer

Heat transfer in rotating cavities determines the thermal stresses and the thermal expansion of the compressor rotor. The heat transfer is dominated by buoyancy-induced convection. Experimental and computational studies have established correlations between the shroud Nusselt number, Nu, and the Grashof number, Gr. Bohn et al. [6] measured the shroud heat transfer in three closed cavities, showing that Nu can be correlated to Gr with an exponent $0.21 < m < 0.23$. Bohn and Gier [25] then corrected the correlation to account for heat losses from the discs, increasing the exponent to 0.3. Simulations by Sun et al. [5] achieved good agreement with these correlations, while calculations by King et al. [7] and Pitz et al. [10] overestimated the shroud heat transfer with $m \approx 0.33$. Saini et al. [26] obtained reduced shroud heat transfer using a compressible code. Gao et al. [27] used a compressible code to determine $m = 0.286$, which was close to the results of Bohn and Gier [25]. Tang and Owen [4] assumed an exponent of 0.25 and achieved good agreement with Bohn et al. [6]. The reduced experimental exponent from Bohn et al. was attributed to the radial temperature rise in the fluid core caused by the effect of compressibility.

Long and Childs [28] used data collected from the open cavity rig at the University of Sussex to derive a Rayleigh-Bénard equation that sums two Gr terms with exponents of 0.25 and $0.\bar{3}$ to determine Nu. Tang and Owen [29] used an exponent of 0.25 to find good agreement between measured and predicted temperature increases of the throughflow. Jackson et al. [30] presented shroud heat transfer measurements collected from the Bath compressor cavity rig; the magnitude of Nu was found to be similar to the correlation for laminar free convection on flat plates. Gao and Chew [23] simulated the open cavity setup from the University of Bath and found an exponent of 0.37 to fit all investigated cases.

In summary, there is a substantial variation in existing correlations for the scaling laws of the Nusselt number. There is a lack of systematic discussion on the differences in shroud heat transfer between open and closed cavities. It is unclear whether the correlations, which are normally established from steady-state cases, are applicable to transient operating cycles, or whether they exhibit stable behaviour. Shroud heat transfer measurements under transient operating conditions for both open and closed cavities are presented here for the first time, providing a large database to investigate the effects of cavity configuration and operating conditions.

2.3 Transient Experiments

As discussed above, while there is experimental and simulation data available for steady-state conditions, there is little published research investigating transient phenomena. Rozman et al. [31] provide a broad review of transient effects in aircraft and industrial gas turbines. In the compressor, there are clearance variations due to the relative mechanical and thermal expansion of the compressor discs and casing, the latter with smaller thermal mass and subjected to more extreme heat transfer. Atkins [2] used the Sussex multi-cavity compressor rig to demonstrate how a relatively small radial inflow can reduce the thermal-response time constants of the rotating discs. The experiments were fully scaled in a dimensionless manner to engine conditions. A lumped-capacitance model was used to illustrate the potential benefits to the engine designer. In earlier work, Burkhardt et al. [32] conducted heat transfer experiments in a five-cavity compressor drum rig. They investigated the effects of changing rotational speed for different steady throughflow mass flow rates and the effects of the throughflow swirl using a co- or contrarotating inner shaft. Variations in the radial distributions of Nu between the upstream and downstream discs were measured when changing rotational speed.

3. EXPERIMENTAL RIG, INSTRUMENTATION AND METHODOLOGY

The Bath Compressor Cavity Rig simulates a generic axial compressor at fluid-dynamically scaled conditions, specifically designed to generate heat transfer of practical interest to the engine designer and validate computational codes. A detailed description of the facility and its capability is provided by Luberti et al. [33]. This paper presents the first transient information collected. This section provides an overview of the essential features of the rig and the data acquisition system.

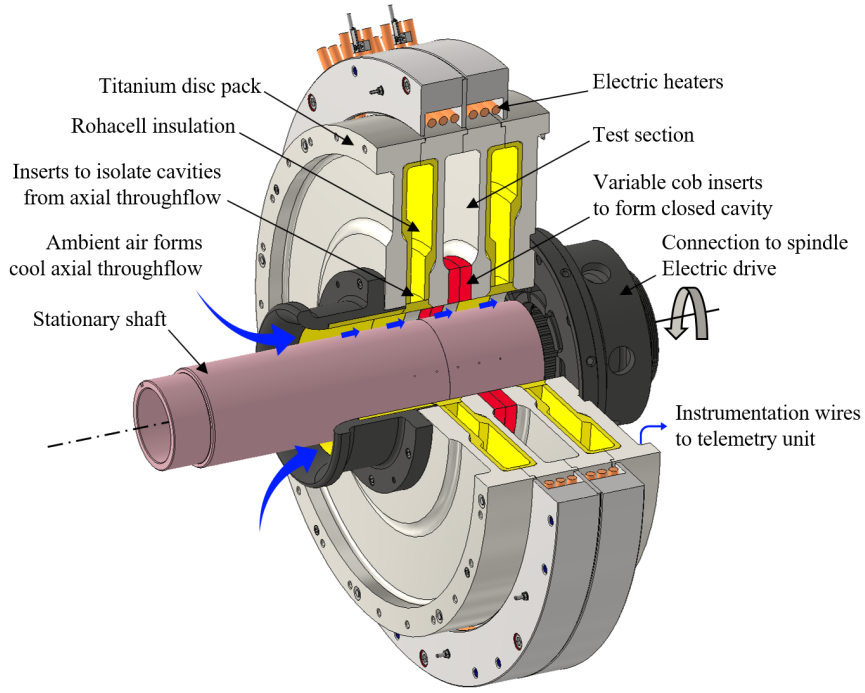

Figure 4: Bath Compressor-Cavity Rig disc drum and test section. Variable cob inserts (shown in red) allow for modifying cavity geometry. Removing the inserts creates open cavity configuration.

Figure 4 shows the disc drum assembly, overhung on a central shaft driven by an electric motor. The test section comprises four titanium discs, which form three inter-disc cavities. The two outermost cavities are lined with Rohacell insulating foam, creating quasi-

adiabatic boundary conditions for the discs in the central cavity. Mass transfer to and from the outer cavities is prevented by removable Rohacell inserts. Separate aluminium ring attachments change the axial gap between the cobs, including the formation of a closed cavity. The shroud and hub radii are 240 and 109 mm, respectively. The disc diaphragm of constant thickness extends between radii 124 mm to 235 mm.

Ambient air for the axial throughflow is drawn from the laboratory through a bell-mouth inlet into the annulus between the stationary shaft and the cobs of the rotating discs. The air is monitored with a thermal mass flow meter with $\pm 5 \times 10^{-4}$ kg/s accuracy (the extraction unit is capable of creating a throughflow rate of up to 0.15 kg/s). The electric motor driving the drum assembly is connected to the main shaft via a belt drive geared to achieve disc rotational speed up to 8,000 rpm. The speed is controlled by a motor encoder with ± 10 rpm accuracy. Six circular 2 kW heater filaments at the rig periphery were used to control the temperature of the shroud. This temperature is limited to 100°C, resulting in a maximum value of $\beta\Delta T$ of approx. 0.2 and 0.25 for closed and open cavities, respectively. Windage heating is significant at high rotational speeds. A sliding mechanism was used to translate the heater assembly axially from the test section to reduce windage in chosen transient experiments.

As illustrated in Figure 5, the test section is equipped with 64 K-type thermocouples embedded in circumferential grooves in the discs and shroud forming the central cavity. The slot grooves were designed to span an isotherm at a constant radius. The thermal-disturbance error was minimised by using the smallest size of slot possible and the use of an epoxy resin with thermal properties that best matched the titanium. An additional thin-foil thermocouple was used to set the temperature on the outside surface of the shroud. The shroud heat transfer was measured using an RdF 27160-C-L-A01 thermopile heat flux gauge, calibrated using the method described by Pountney et al. [34]. Thermocouples to determine the temperature of the axial throughflow were located on three rakes mounted on the stationary shaft, one upstream of the disc drum and two near the cobs of the test cavity. The rakes have a slim cylindrical section to minimise flow disruption.

The cyclical pressure variation of the cavity flow structure was measured using two fast-response Kulite XCQ-080 sensors, mounted flush with the surface of the downstream disc at $r/b = 0.85$. The sensors were separated circumferentially by $\gamma = 35°$. The cross-correlation of the data from the two sensors enabled the calculation of the number of vortex pairs and their speed relative to the disc. The method of data analysis is described in detail by Jackson et al. [16]. This analysis method is extended for the transient experiments in Section 4.1.

The wiring for all rotating instrumentation was routed to the back surface of the disc drum and passed to a Datatel telemetry unit, which transmits the data to a stationary receiver. Thermocouple data was collected at 1-10 Hz. This was converted to a temperature using cold-junction measurements from PT100 Resistance Temperature Detectors and a known calibration. The overall measured temperature uncertainty is estimated to be ±0.5°C. Data from the heat flux gauge were sampled at a higher rate (10 kHz) and filtered using a bandpass filter. Data from the high-frequency Kulite pressure sensors was acquired by a National Instruments NI 9215 data logger at a sampling rate of 10 kHz. The sampling time during transient experiments was 3600 seconds – 600 seconds of a steady-state condition followed by 3000 seconds over the transient period. Signal aliasing was minimised by a 1 kHz low-pass filter. Since the highest rotational frequency of the disc is 133 Hz (8,000 rpm), and the relative speed of the rotating structures is less than this, the acquisition and filtering frequencies were sufficiently high to satisfy the Nyquist criterion. The pressure measurement uncertainty is estimated to be ±1.5 mbar.

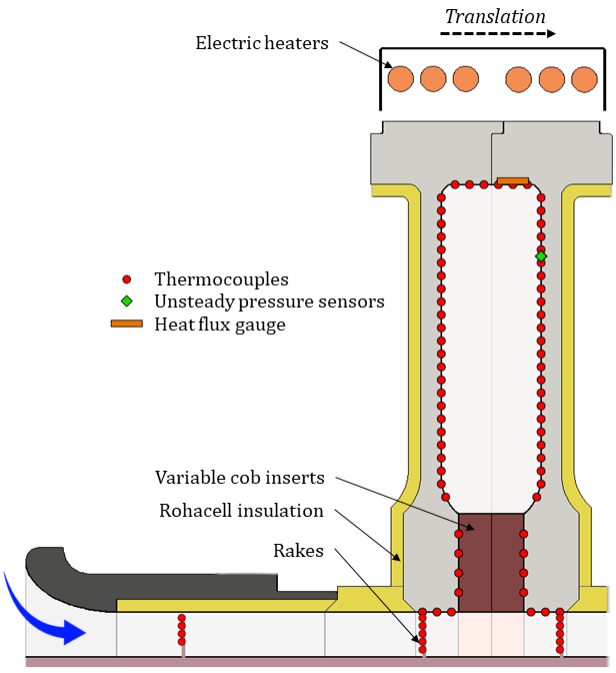

Figure 5: Test section instrumentation

All transient experiments start from steady-state conditions, defined as when locally-measured temperatures vary by $< 0.1°C$ within a ten-minute interval. Three types of transient experiments were conducted: *shroud-temperature*, *speed* and *Rossby* transients. For the *shroud-temperature* transients, the electrical power to the heater filaments was stopped at constant disc speed, reducing the heat flux through the shroud from a prescribed steady-state setting of $\beta\Delta T$; windage could be minimised but not eliminated, with $\beta\Delta T \rightarrow 0$ at the end of the transient. For the *speed* transients, the heater power was kept constant; due to mass inertia and limited torque, accelerations and decelerations of the discs were limited, *e.g.* approximately 1.5 minutes to accelerate from 2000 to 8000 rpm. The mass flow rate of the axial through-flow was changed for the *Rossby* transients at a constant rotational speed and heater power; typically the changes in Ro occurred in less than 3 seconds.

Ideally, the transients created in the rig should accurately simulate an engine cycle and isolate the individual effects of Ro, $\beta\Delta T$, χ and Re_ϕ. Here the experimental data from the transients interrogate the changes in cavity flow structure, provide nondimensional heat transfer correlations, and have been used to validate theoretical models in Nicholas et al. [35]. From a practical perspective, these models can be scaled to the engine and used to inform thermo-mechanical design codes and methods.

In total, 40 transient experiments were conducted over a range of engine-representative conditions. In the Appendix, Tables 1 and 2 summarise the main non-dimensional parameters for the cases presented in this paper.

4. DATA ANALYSIS

4.1 Pressure Data Analysis

4.1.1 Buoyancy-induced Flow Structures. Transient frequency analysis of the pressure data was performed to evaluate the changing magnitude and relative speed of the rotating structures with time. First, the amplitude and frequency of the principal modes

were found from the Fast Fourier Transform (FFT). A five-second sample size was chosen for the FFT analysis – sufficiently long for good fidelity, but short enough to capture the transient behaviour. The time is presented as a Fourier number (Fo), where Fo = 0 defines the start of the transient.

$$\mathrm{Fo} = \frac{\alpha t}{b^2} \tag{1}$$

The pressure coefficient is defined by the normalised pressure difference between the sample and the time average.

$$C_p = \frac{p - \bar{p}}{\frac{1}{2}\rho_f \Omega^2 b^2} \tag{2}$$

The frequency of the measured signal, f, was normalised by the rotational frequency of the discs f_d to translate the data into the rotating frame of reference. The output from the analysis is shown in Section 5 in the form of FFTs and spectrograms. The frequency of the fundamental modes shown in an FFT was used with the cross-correlation method described by Jackson et al. [16] to determine the relative speed (or 'slip') of the rotating core, where the dominant frequency is divided by the number of structures, n. The dominant peak in an FFT was observed to shift during a transient, which can be an effect of a change in individual structure slip, or a change in the number of structures. Depending on the rotational speed, three to four vortex pairs were measured using the closed cavity configuration, while only one vortex pair was found in all open cavity tests. The slip of individual structures was typically about 1% or 15% for closed and open cavities, respectively.

A spectrogram can be used to visualise the transient phenomena. This was created from a series of FFTs, where the data was sampled over periods that overlap with adjacent FFTs. This demonstrated the gradual change in frequency spectra with time. For all spectrograms, the period for this sampling process was 5 s, with an overlap region of 93% of the window. Spectrograms are presented with corresponding FFTs in Section 5. The fundamental frequency mode corresponds to a peak in C_p. The frequency and intensity of this peak changes with time, indicative of a change in slip and strength of the rotating structures.

4.1.2 Plume Mass Flow Rate. Lock et al. [17] investigated the unsteady flow characteristics in a closed cavity, identifying coherent rotating structures across a range of experimental conditions. These cyclonic / anti-cyclonic vortex pairs generate the non-dimensional circumferential pressure difference necessary for the radial outflow (of cold fluid) and inflow (of hot fluid) through the rotating core – see Figure 3. The experiments showed the magnitude of these pressure variations could be correlated against shroud heat transfer, characterised by Gr_s, and that at high values of χ the structures did not exist. This is true for both open and closed cavities, as heat transfer from the shroud to the core is driven by radial plumes between vortex pairs for both configurations. The non-dimensional mass flow rate in the plumes was correlated as follows:

$$C_w = \frac{\dot{m}}{\mu s} = \frac{n \mathrm{Re}_\phi C_{\Delta p}}{2} = B(\mathrm{Ra}_s)^m \tag{3}$$

where $\dot{m}$ is the plume mass flow rate and B and m are empirical constants. The pressure coefficient in Equation 3 is defined by the maximum-to-minimum pressure difference between the anti-cyclonic and cyclonic vortices, Δp:

$$C_{\Delta p} = \frac{\Delta p}{\rho_c \Omega_c^2 b^2} \tag{4}$$

The pressure difference is determined by fitting a sinusoidal curve to the circumferential pressure distribution from the unsteady sensors and accounts for the asymmetry of the vortices. For both steady-state and transient cases, the fitted Δp for every structure revolution and both sensors were averaged to determine the plume mass flow rate.

4.2 Transient Plume Model for Heat Transfer

Measurements of the temperature of the rotating fluid in the cavity were not possible in the current experimental arrangement. Shroud heat transfer correlations appropriate for fluid-dynamic scaling require knowledge of the core temperature near the shroud. Tang and Owen [36] used a conjugate model for a closed rotating cavity to determine the radial variations of the temperature of the discs and fluid core, accounting for the effects of compressibility. The titanium discs are relatively thin and the temperature distribution was determined by one-dimensional conduction using the general fin equation with an adiabatic back surface. A new iteration of the conjugate model from Nicholas et al. [35] is used here, which calculates transient core temperatures using a two-dimensional (2D) Finite Element Analysis (FEA) solver for conduction through the discs. This accounts for the (previously ignored) heat loss through the discs that affects the resultant radial distribution of the fluid core. The model accounts for this with a convective heat transfer boundary condition on the Rohacell insulation surface, with heat transfer coefficients equal to that of the central cavity discs. This boundary condition is referenced to the neighbouring cavity core temperature, assumed equal to an intermediate value lower than that of the central cavity. However, the solution was found to be relatively insensitive to this value, with a 10% change in its non-dimensional temperature resulting in less than 1% change in modelled disc temperature. The experimentally-derived (or *optimised*) core temperatures are then obtained from the model by matching the calculated disc temperatures with those given by experiments - both for the closed and open cavity, and both steady-state and transient conditions.

The shroud Nusselt number is defined as:

$$\mathrm{Nu}_s = \frac{q_s s/2}{k(T_s - T_{c,s})} \tag{5}$$

Here q_s is the experimentally-measured shroud heat flux, T_s the experimentally measured shroud temperature, and $T_{c,s}$ the temperatures of the core near the shroud determined from the model; these are all changing with time through the transient. Other parameters are defined in the nomenclature. Both the shroud Nusselt number and the plume mass flow rate (Equation 3) are correlated to the shroud Grashof number:

$$\mathrm{Gr}_s = \frac{\rho_{c,b}^2 \Omega^2 b}{\mu^2} \left(\frac{s}{2}\right)^3 \beta \left(T_s - T_{c,b}\right) \tag{6}$$

A term for non-dimensional heat flux is also given:

$$\psi = \frac{2b^2 q}{k_d t_d (T_{s,max} - T_{ref})} \tag{7}$$

where t_d is the disc diaphragm thickness, $T_{s,max}$ is the maximum shroud temperature in the transient (usually the starting steady-state value) and T_{ref} is the starting average temperature of the axial through-flow upstream of the cavity.

5. TRANSIENT HEAT TRANSFER AND FLOW STRUCTURE

5.1 Closed Cavity Shroud Temperature Transient – minimum windage

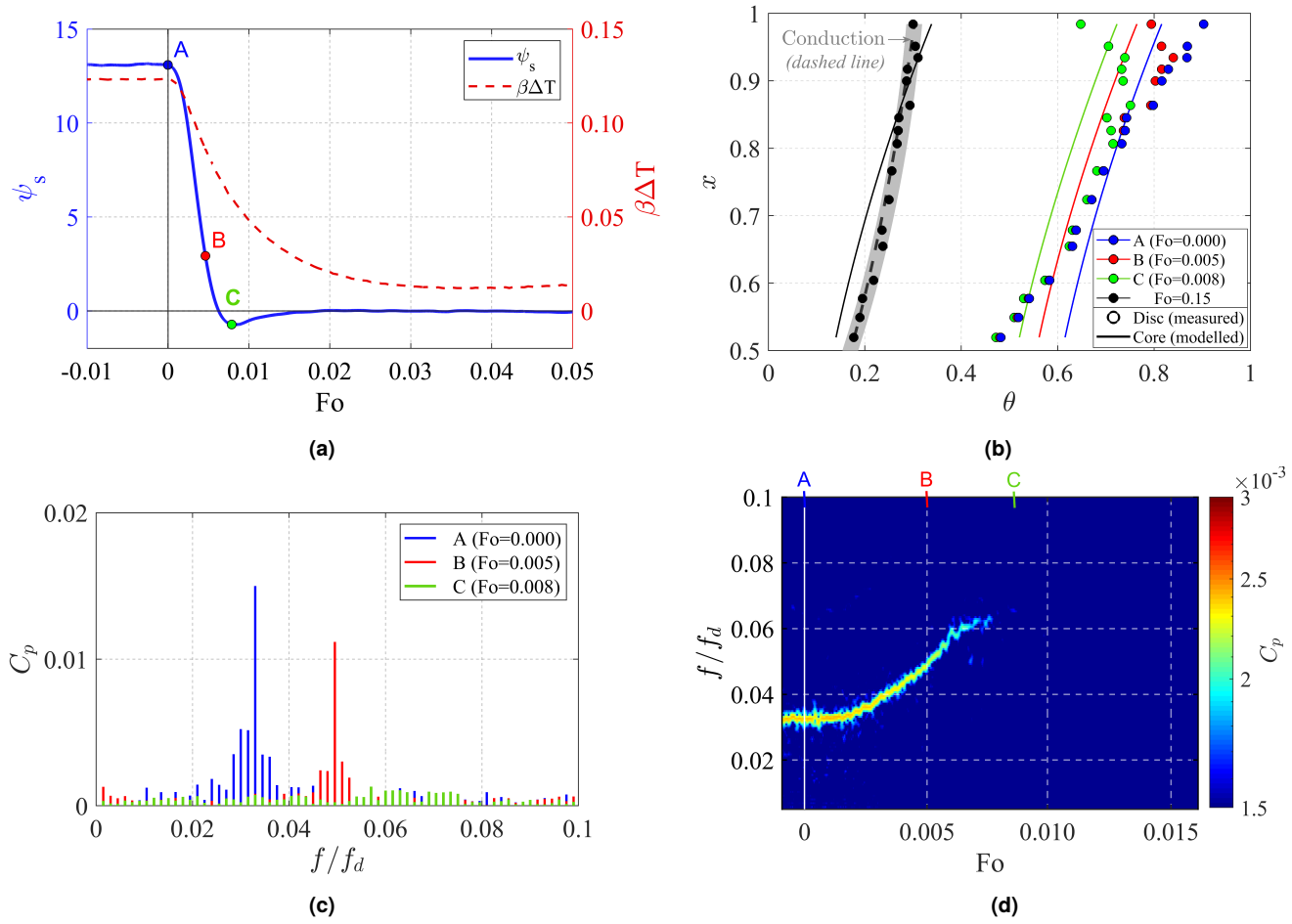

Figure 6: Shroud temperature transient in closed cavity with minimised windage for Case D_1. (a) Variation of non-dimensional heat flux with Fo, (b) radial distribution of disc (measured - points) and core (modelled - lines) temperatures at different Fo; dashed line is pure conduction solution for disc temperature; shaded region shows 95% confidence interval for temperature measurements, (c) FFT of the unsteady pressure in the cavity at different Fo in the rotating frame of reference, (d) spectrogram.

Figure 6a illustrates the variation of shroud heat flux, ψ_s, and $\beta\Delta T$ with Fo for a *shroud-temperature* transient in the closed cavity. This is Case D_1 from Table 1 (see Appendix for details). Three points (A-C) mark significant values of Fo where radial distributions of temperatures (Figure 6b) and FFTs (Figure 6c) are illustrated; the spectrogram is shown in Figure 6d.

In this transient, the power to external shroud heaters was shut off abruptly and the assembly traversed axially to minimise windage heating. This action creates a decrease in measured shroud heat flux and $\beta\Delta T$ from the steady-state value (A) at Fo = 0. There is a corresponding reduction in shroud and disc temperature at high radius, while the disc temperature at lower radii responds less rapidly. The difference in the transient temperature profiles at high and low radii is due to the varying thermal responses of the shroud and hub – the shroud cools more rapidly due to the cooling at the periphery. The maximum disc temperature moves radially inwards with increasing

Fo as the disc cools.

At Fo > 0.007, $\psi_s < 0$ and $\psi_s \to 0$ asymptotically at large Fo. This measured negative heat flux is a physical phenomenon where the metal temperature at the shroud has cooled below the core temperature near the shroud, i.e., $\theta_s < \theta_{c,s}$ as shown in Figure 6b. Under these circumstances, the shroud heat transfer is dominated by conduction from the core to the shroud, not convection from the shroud. The core temperature increases with increasing radius, being dependent not only on the heat transfer from the discs but also on the compressibility parameter, χ. At large Fo, the disc temperature approaches the radial distribution corresponding to one-dimensional conduction in a cylinder (dashed line at Fo = 0.15):

$$\theta_d = \frac{\ln(x/x_i)}{\ln(x_o/x_i)}(\theta_{d,o} - \theta_{d,i}) + \theta_{d,i} \tag{8}$$

As shown in Figure 6b, at Fo = 0.15 there is still heat transfer from the core to the discs at high radius and heat transfer from the discs to the core at lower radii. Due to windage, $\beta\Delta T$ is not zero.

As stated in Section 3, the estimated temperature measurement uncertainty is ±0.5°C. Following the methodology presented in Luberti et al. [33], it is more meaningful to present the uncertainty as the 95% confidence interval of the disc temperatures reproduced by the Bayesian method described by Tang et al. [37]. The confidence interval is shown for the temperature distribution as the shaded area at the end of the transient in Figure 6b. The uncertainty does not change significantly between experiments. For the purpose of clarity the confidence interval is omitted for subsequent sets of data.

The unsteady transient pressure provides information about the cyclonic/anti-cyclonic flow structure inside the rotating core and the number of vortex pairs (n). Figure 6c shows an FFT of pressure signals corresponding to A, B and C (i.e., Fo = 0, 0.005 and 0.008, respectively). At Fo = 0 (steady-state), the passing frequency of a single vortex pair, $f_{s,1}$, is shown by the peak and equals approximately 3% of the disc rotational frequency, f_d. Throughout the transient $n = 4$ pairs of structures were measured until they vanished. The relative rotational speed of the flow structures is $f_s = f_{s,1}/n$, with the difference between the disc and core rotation (or *slip*) measured to be < 1% (i.e., near solid-body rotation) in the closed cavity. The principal frequency on the FFT is not a unique value, but a peak over a narrow range of frequencies. This indicates small but persistent variation in slip associated with an aperiodic unsteadiness in the structures, even in steady state. The slip of the structures increased through the transient while the magnitude of these pressure variations, C_p, decreased as the relative strength of buoyancy-induced convection reduced as $\psi_s \to 0$. This is the opposite trend to one reported by Jackson et al. [16], who showed a decrease in the slip when $\beta\Delta T$ decreases. This difference can be attributed to different disc temperature distributions between the transient and steady-state conditions. During a *shroud-temperature* transient there is a region of disc temperature reducing with increasing radius, as visible in Figure 6b. This does not occur in steady-state conditions, where there is a persistent trend of increasing disc temperature with increasing radius regardless of $\beta\Delta T$. Different temperature distributions result in a different equilibrium of energy and momentum transfer, which in turn affects the vortex slip. Structures were not detected for Fo ≥ 0.008. The spectrogram (Figure 6d) illustrates the increase in slip and the vanishing of the vortex structures.

5.2 Open Cavity Shroud Temperature Transient — minimum windage

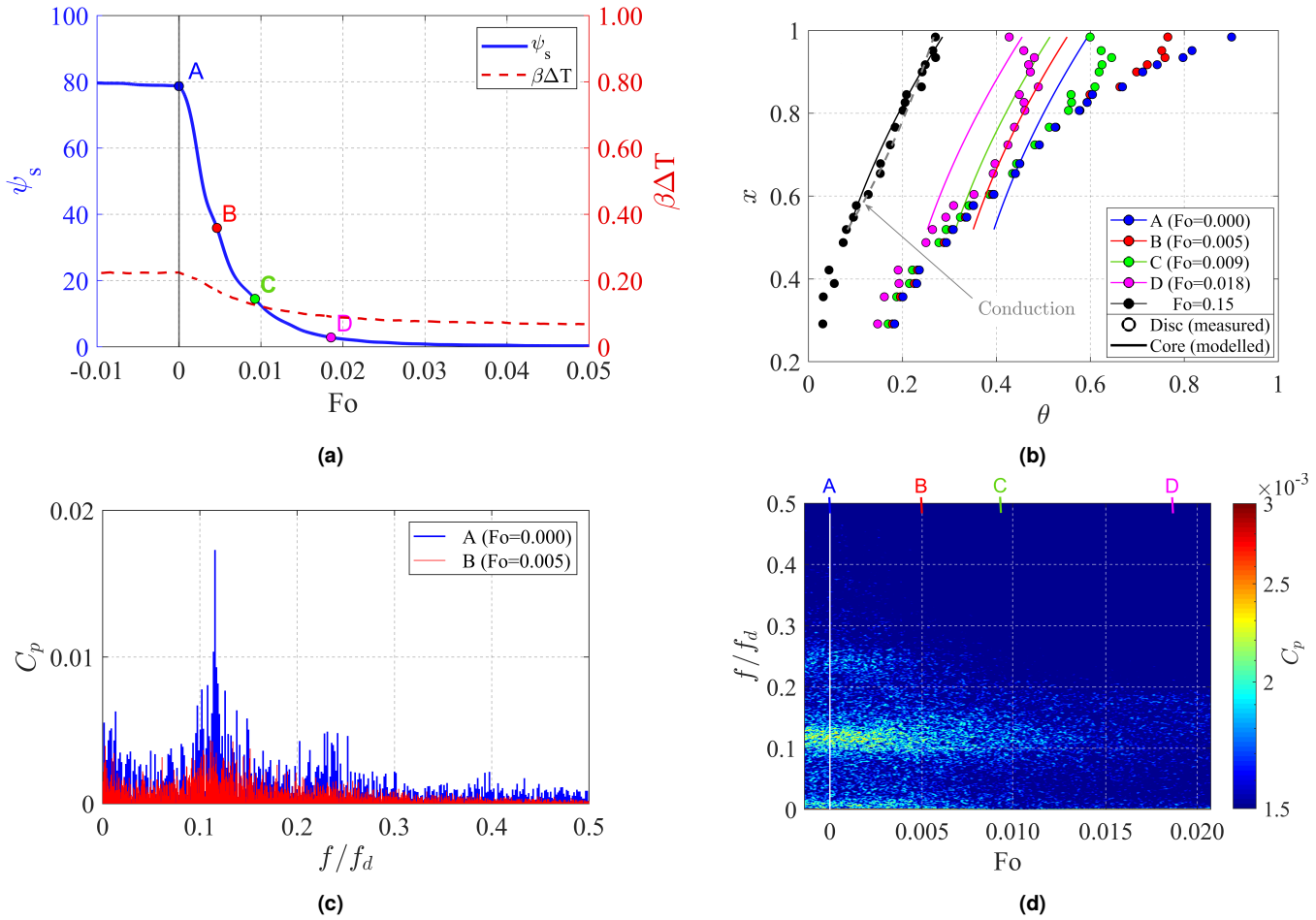

Figure 7: Shroud temperature transient in open cavity with minimised windage for Case N_1. (a) Variation of non-dimensional heat flux with Fo, (b) radial distribution of disc (measured - points) and core (modelled - lines) temperatures at different Fo; dashed line is pure conduction solution for disc temperature, (c) FFT of the unsteady pressure in the cavity at different Fo in the rotating frame of reference, (d) spectrogram.

Figure 7 illustrates the heat transfer and fluid-dynamic phenomena for a *shroud-temperature transient* in the open cavity with an axial throughflow at Ro = 0.2. This is Case N_1 from Table 2 (see Appendix for details). Four positions (A-D) at Fo = 0, 0.005, 0.009 and 0.018 mark significant times where radial distributions of disc and core temperatures and FFTs are illustrated.

There are similarities with the closed cavity (Figure 6), but the differences for the open cavity case are discussed here. At the same Re_ϕ and shroud temperature, the steady-state (Fo $\leq$ 0, position A) magnitudes of ψ_s and $\beta\Delta T$ are larger for the open cavity, due to the enthalpy exchange with the throughflow. This is reflected in the larger gradient in the radial distribution of disc temperature, with lower temperatures at low radius.

In this transient, the external shroud heat supply was again shut off abruptly and the assembly on the periphery of the test section traversed axially to minimise windage heating. At low radius there is significant cooling from the axial throughflow. The shroud heat flux decreases during the transient but, contrary to the closed cavity case, ψ_s reduces to zero without changing sign. The ingestion and enthalpy exchange with the throughflow means the core temperature near the shroud is less than the metal temperature, i.e., $\theta_s > \theta_{c,s}$, as shown in Figure 7b. However, $\theta_s \rightarrow \theta_{c,s}$ at large Fo and convective heat flux (and consequently the main driver for buoyancy-induced

flow) diminishes. At large Fo the core and disc temperatures are similar and again approach the radial distribution corresponding to one-dimensional conduction in a cylinder (see Equation 8).

Note that the experimental measurements of disc temperature extend to the cob region, but core temperature predictions are limited to the diaphragm section of the disc. The heat flux reaches zero more rapidly in the closed cavity configuration as the core fluid temperature is determined by the hub temperature instead of the axial throughflow temperature and the compressibility effect raises the core fluid temperature at high radius, i.e., $\theta_{c,s}$ is always larger for the closed cavity (for the same Re_ϕ).

Figure 7c is an FFT of pressure signals corresponding to times A (Fo = 0) and B (Fo = 0.005). The signals were too weak to be resolved coherently for Fo > 0.005. Unlike the closed cavity, just a single pair ($n = 1$) of cyclonic/anti-cyclonic vortices was measured. This is consistent with Jackson et al. [22], who detected harmonic modes caused by unequal-sized vortices, with the cyclonic vortex the larger of the pair. The coherency, strength and slip (typically 10 to 15%) of the rotating structures relative to the disc increased as the buoyancy forces increased in dominance. In Figure 7c the frequency is normalised by the rotational frequency of the disc. At Fo = 0 both pressure sensors measured a dominant signal at 12% of the disc speed and a minor peak at twice this frequency due to the asymmetry of the vortex intensity. The strength of the vortex pair (i.e., the magnitude of peak C_p) reduced significantly at Fo = 0.009 as the shroud heat flux and buoyancy forces decay through the transient. The slip of the structures remained constant. The spectrogram (Figure 7d) shows clearly this unchanging frequency and the minor peak located at about $f/f_d = 0.25$. The intensity of both vortices is observed to decay with increasing Fo, with the minor peak vanishing earlier than the dominant peak. The magnitude of the slip has practical consequences for the engine designer as it influences surface shear forces, internal windage and the power required to drive the compressor.

5.3 Closed Cavity Shroud Temperature Transient with windage heating

Figure 4 illustrates the test section and the electric heater assembly at the periphery of the test section. Transient experiments were conducted at constant rotational speed with the external shroud heater power shut off abruptly at Fo = 0, but the assembly was not traversed away so windage was significant. Figure 8 illustrates the heat transfer and fluid-dynamic phenomena for this case in the closed cavity without windage minimised. This is Case D_2 from Table 1. Four points (A-D), at Fo = 0, 0.009, 0.018 and 0.138, mark significant times where the radial distributions of disc and core temperatures, and FFTs are illustrated. The heat flux and $\beta\Delta T$ reduce rapidly at low Fo. However, the windage heat flux that persists is sufficient to maintain buoyancy-induced flow in the cavity. The transient correspondingly features a change from the initial steady-state condition at Fo = 0 to a second steady-state condition at large Fo, where the heat flux to the shroud is entirely due to windage.

The radial distribution of disc and core temperatures are shown in Figure 8b. At all Fo, $\theta_s > \theta_{c,s}$ and conductive heat flux from the shroud creates buoyancy-induced flow. Contrary to the previous two cases, the shroud heat flux does not reduce to zero even though $\beta\Delta T$ decreases as the shroud cools. Figure 8c is an FFT of pressure signals corresponding to positions A-D. Throughout the transient $n = 4$ pairs of structures were measured. The rotational speed of the flow structures relative to the disc (slip), $f_s = f_{s,1}/n$, increased during the transient (at B and C) but returned to approx. 1% (i.e., approximately solid-body rotation) at D near the final steady-state condition at reduced $\beta\Delta T$. Consistent with the plume model [36] and Equation 3, the magnitude of C_p decreased as $\beta\Delta T$ decreased. The spectrogram (Figure 8d) illustrates these effects and shows structure persistence at large Fo.

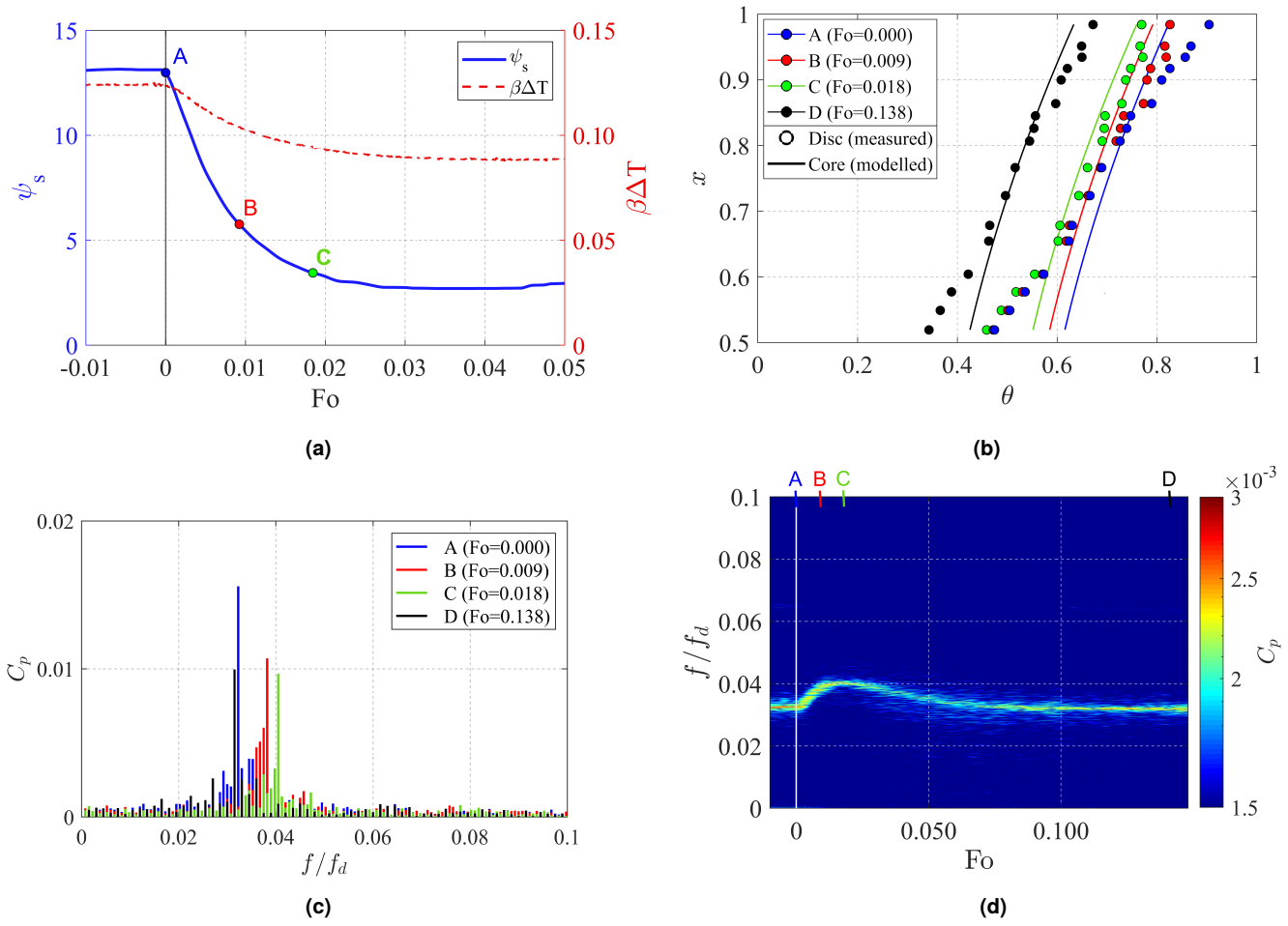

Figure 8: Shroud temperature transient in closed cavity with significant windage for Case D_2. (a) Variation of non-dimensional heat flux with Fo, (b) radial distribution of disc (measured - points) and core (modelled - lines) temperatures at different Fo, (c) FFT of the unsteady pressure in the cavity at different Fo in the rotating frame of reference, (d) spectrogram.

5.4 Closed Cavity Speed Transient

A series of experiments were conducted using the closed cavity configuration to simulate changes in disc speed during engine accelerations and decelerations. Here the heater power was kept constant while the rotational speed of the disc drum was varied from a steady-state condition. In the acceleration, the disc speed changed from 2000 rpm ($\mathrm{Re}_\phi = 0.8 \times 10^6$) to 7000 rpm ($\mathrm{Re}_\phi = 2.7 \times 10^6$), and the reverse for the deceleration. This is case G in Table 1.

Figure 9 illustrates three points (A-C), at Fo = 0, 0.005 and 0.018, marking significant times where the radial distributions of disc and core temperatures, and FFTs are illustrated. Due to mechanical inertia, the change in speed is not instantaneous and the disc accelerates for $0 < \mathrm{Fo} < 0.005$. The increase in Re_ϕ creates an increase in Gr and χ. The heat flux increases but there is a competing mechanism: increased Reynolds number but an increased core temperature near the shroud due to an increased effect of compressibility at high rotational speed. The radial variation of the disc temperature (shown in Figure 9b) is seen to be almost invariant throughout the transient. However, the core temperature shifts from an almost isothermal profile at low rotational speed (low χ) to one with a significant increase with radius at high rotational speed (high χ); this reduces $\theta_s - \theta_{c,s}$ with increasing Fo until a new steady-state condition is reached at large Fo. The steady-state condition (at equal heater power to the periphery of the rig) is also influenced by increased windage at the

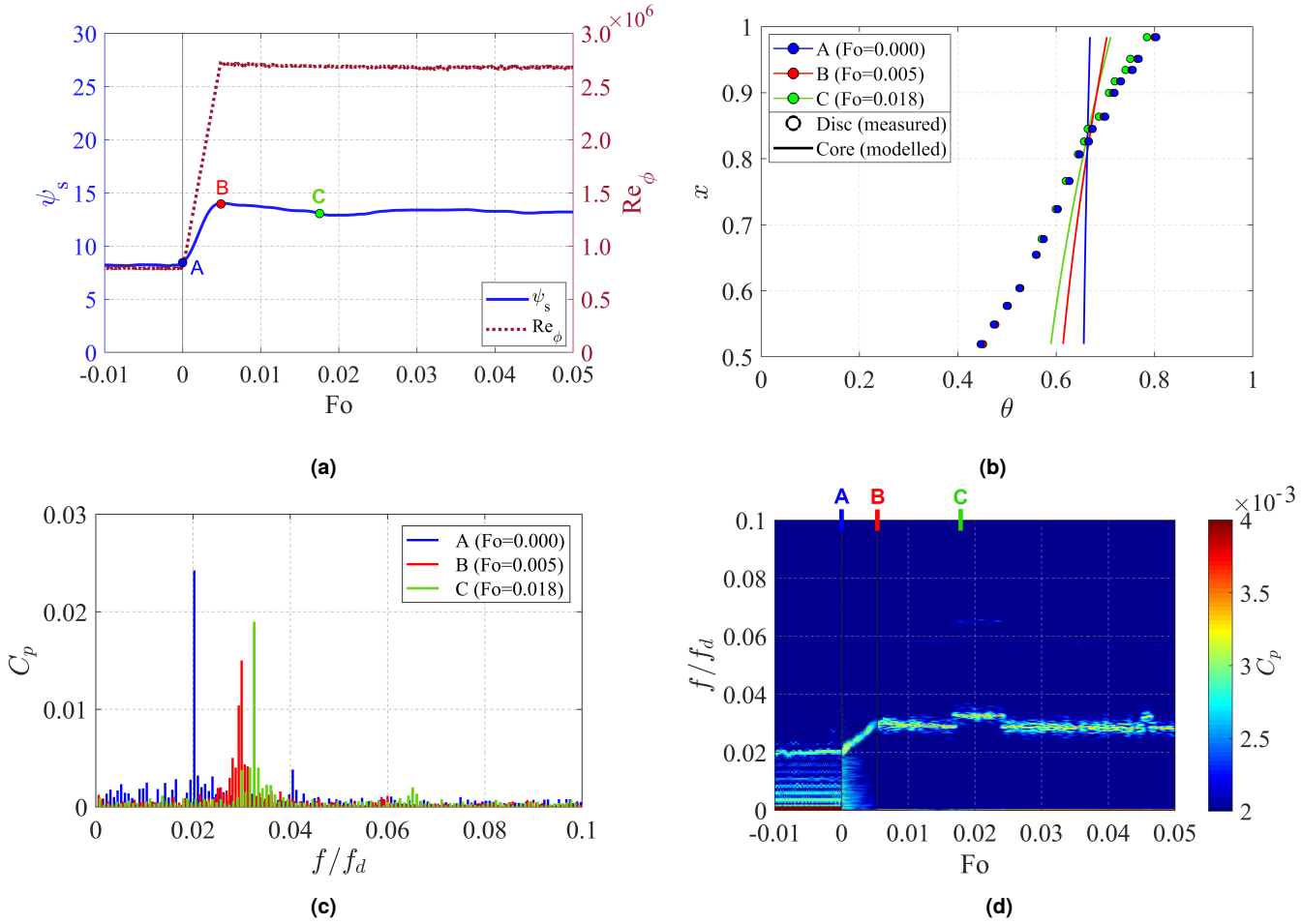

Figure 9: Accelerating speed transient in closed cavity for Case G. (a) Variation of non-dimensional heat flux with Fo, (b) radial distribution of disc (measured - points) and core (modelled - lines) temperatures at different Fo, (c) FFT of the unsteady pressure in the cavity at different Fo in the rotating frame of reference, (d) spectrogram.

higher rotational speed. Throughout the transient, $\theta_s > \theta_{c,s}$ and buoyancy-induced flow dominated the flow structure in the cavity.

The FFT of the cyclic pressure signals is shown in Figure 9c for positions A-C, each with clearly defined peaks indicating strong buoyant activity within the cavity. At A (Fo = 0) there are three pairs of vortices in the core ($n = 3$), rotating relative to the disc with 0.7% slip (near solid body rotation). There are also three pairs at B (Fo = 0.005 and higher Re_ϕ) but the slip has increased to 0.9%. However, the buoyancy-induced flow structure is unstable for $0.015 < \mathrm{Fo} < 0.025$ as illustrated in the spectrogram (Figure 9d). In this interval the number of structures varied between $n = 3$ and $n = 4$, settling to $n = 3$ at large Fo. The slip in this interval is constant but the rotational speed of the flow structures is $f_s = f_{s,1}/n$, which causes a shift in the spectrogram. Note that the measured number of pairs at this Reynolds number is consistent with steady-state measurements of Jackson et al. [16], who observed $n = 3$ for $\mathrm{Re}_\phi < 2.2 \times 10^6$ and $n = 4$ for $\mathrm{Re}_\phi > 2.5 \times 10^6$. The new experiments presented here suggest a transitional Re_ϕ for the stability of these unsteady structures. This is in line with the findings of King et al. [7]. Due to limitations in the method of analysis as the disc rotational speed changed, there is some discontinuity in noise for $0 < \mathrm{Fo} < 0.005$ in Figure 9d. This is due to the need for additional calculations over the transient period to account for changing disc passing frequency, forming a composite image.

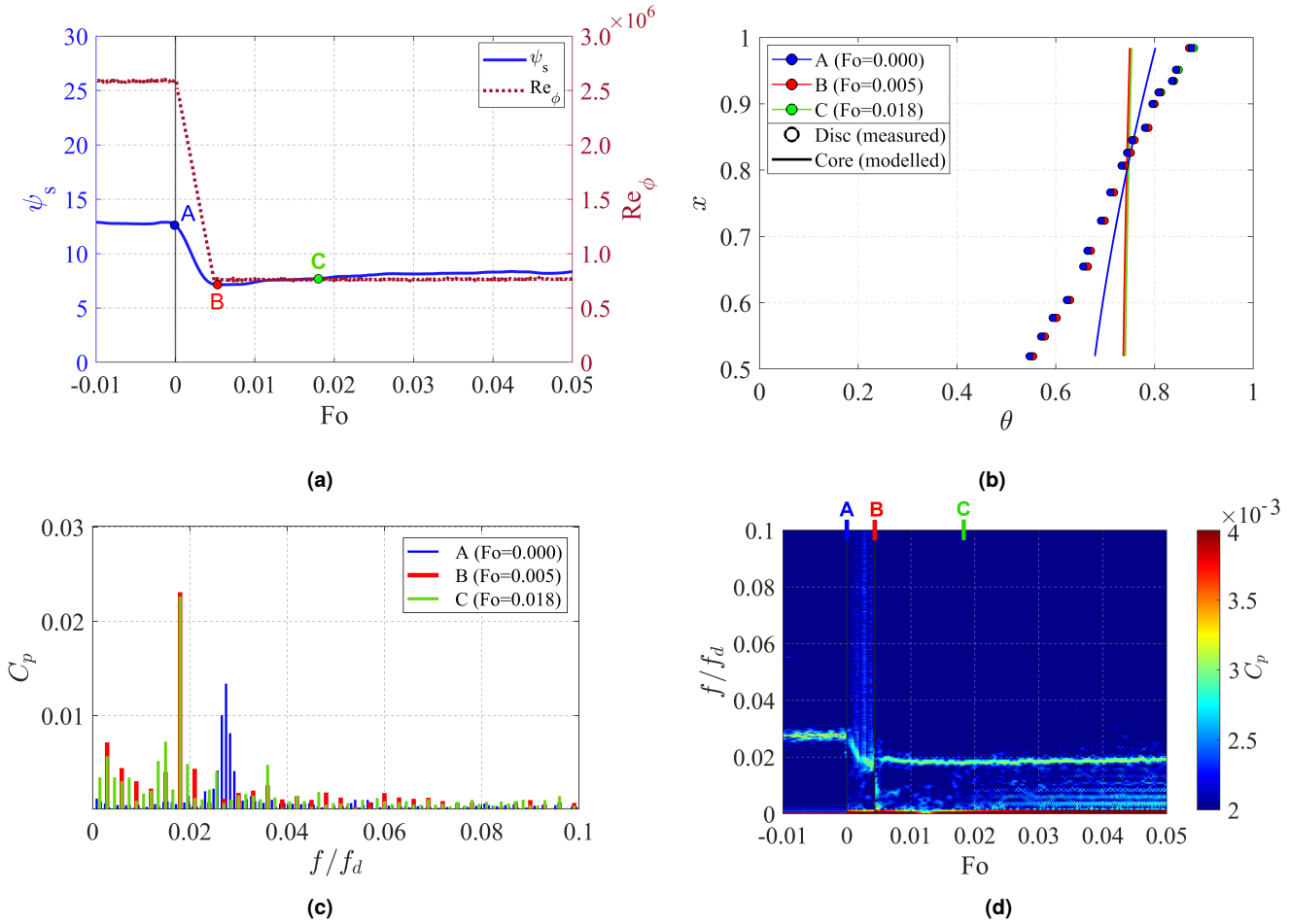

Figure 10: Decelerating speed transient in closed cavity for Case G. (a) Variation of non-dimensional heat flux with Fo, (b) radial distribution of disc (measured - points) and core (modelled - lines) temperatures at different Fo, (c) FFT of the unsteady pressure in the cavity at different Fo in the rotating frame of reference, (d) spectrogram.

Figure 10 illustrates similar effects during deceleration from $\mathrm{Re}_\phi = 2.5 \times 10^6$ to $\mathrm{Re}_\phi = 0.8 \times 10^6$. Positions A and B mark the times for the start and end of the deceleration. The reduction of the rotational speed (and Gr) creates a decrease in shroud heat flux, with the system transforming from one steady-state condition at Fo = 0 to another at large Fo. Compressibility effects are significant at the higher Re_ϕ, where the core temperature increases with radius. Unlike the acceleration, the number of vortex pairs was stable with $n = 3$ throughout the transient. The FFTs and spectrogram show the slip decreases slightly at lower Re, changing from 0.9% to 0.7% of the disc speed on either side of the deceleration. It can be noted in Figures 9c and 10c that the magnitude of C_p is lower at higher rotational speeds. This suggests that despite an increase in Gr, the required non-dimensional circumferential pressure variation decreases for the radial plume mass flow rate.

5.5 Open Cavity Rossby Transient

Figure 11 illustrates the effect of changing the axial throughflow mass flow rate or the Rossby number (at constant disc speed and heating power at the rig periphery) in the open cavity configuration. This is case U in Table 2. The experimental setup allowed for an almost instantaneous (< 3 s) change in Ro from 0.2 to 0.4, with a corresponding abrupt increase in shroud heat flux. The increased ingestion and exchange of enthalpy cooling air at Ro = 0.4 reduced the temperature of the core, leading to an increase in $\theta_s - \theta_{c,s}$

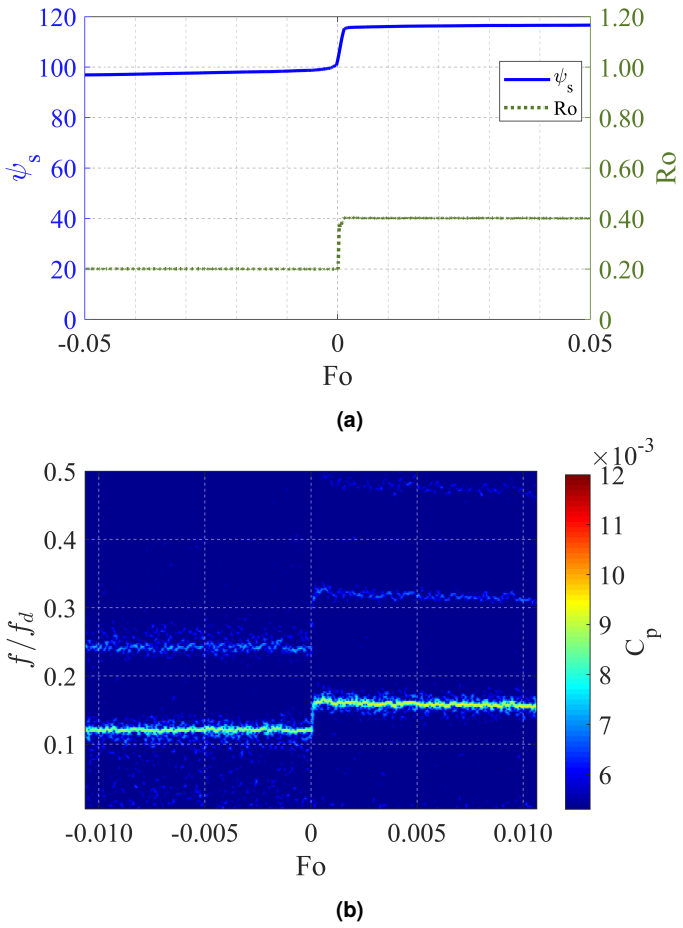

Figure 11: Rossby Transient in open cavity for case U. (a) Variation of non-dimensional heat flux with Fo, (b) spectrogram.

and hence heat flux and Gr. The increased exchange of low angular momentum fluid at increased Ro increased the slip of the rotating structures from 12% to 16%. The spectrogram shows a clear, coherent single pair ($n = 1$) of cyclic structures before and after the transient at Fo = 0. This flow structure remained qualitatively unchanged: the second harmonic peak, indicating vortex asymmetry, shifted proportionally with the primary peak. The magnitude of C_p for the primary peak frequency increased with Ro, as Gr increased and the relative effects of buoyancy became more dominant. As shown in Equation 3, for a fixed Re_ϕ, the plume mass flow rate and thus the pressure variation increases when the shroud Gr increases.

5.6 Steady-State and Transient Shroud Heat Transfer

The practical application of buoyancy-induced flow to engine design requires dimensional analysis and fluid-dynamically scaled correlations of heat transfer, usually in the form of power-law exponents. The shroud Nusselt number, Nu_s, is usually correlated against the shroud Grashof number, Gr_s, or Rayleigh number. Figure 12 shows the shroud heat transfer in the form of Nu as a function of Gr using equations 5 and 6. The transient heat flux at the shroud was determined experimentally and corrected for radiation [38]. The transient temperature of the core near the shroud was determined from the conjugate model [35] described in Section 4.2, which includes a 2D FEA solver for conduction through the discs. The experimentally-derived (or optimised) core temperatures were obtained by matching the calculated disc temperatures with those given by experiments.

The correlations for both the closed and open cavities are illustrated in Figure 12. Consider first the open cavity where both steady-state and transient correlations are shown. The transient data are the first of their kind for compressor cavities, showing that a single correlation can be applied across steady-state and transient conditions. There is remarkable agreement between the correlations from experiments (including the sample cases shown in Tables 1 and 2, as well as past experiments presented by Jackson et al. [16, 22]) across a wide range of Gr. Shroud temperature, speed and Rossby transients all feature in this correlation. Note that transient data were only possible where stable, coherent structures existed in the cavity and the flow was dominated by buoyancy. Only data within the calibrated range of the heat flux gauge was presented. A best-fit correlation was determined using maximum-likelihood estimation (MLE) and found to be $\mathrm{Nu}_s = 0.54\mathrm{Ra}_s^{0.25}$. The 95% confidence limit of the calculated Nusselt numbers is ±11, as evidenced by the relatively large amount of scatter. The data broadly conforms to expectations from dimensional analysis, which determine the dependence of the observable shroud heat transfer parameters in the form of power-law exponents. The correlation is similar to that of laminar free convection. However, the complexity of the fluid dynamics, cavity geometry and heat transfer would suggest that laminar free convection is an unjustified simplification.

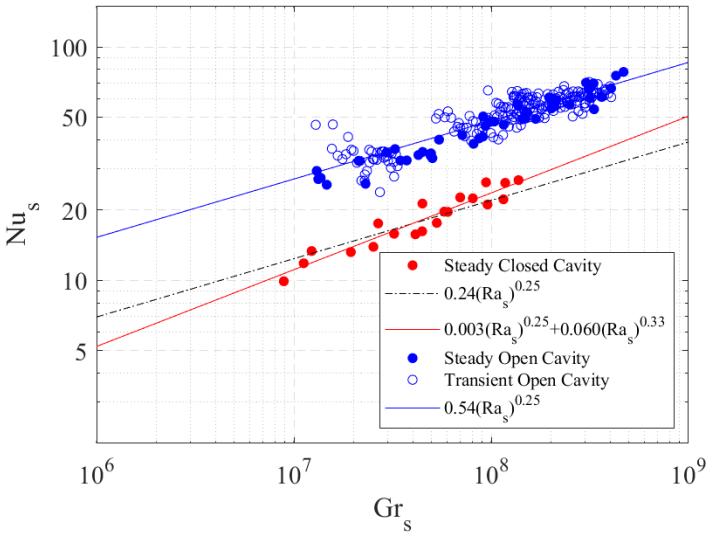

Figure 12: Experimental shroud heat transfer correlation for the open cavity at both steady-state and transient conditions, and the steady-state closed cavity correlation. Based on optimised core temperatures.

The magnitude of shroud heat transfer is weaker in the closed cavity. As such, it is far more sensitive to uncertainties in heat flux measurements during transient experiments, and so only steady-state values are presented here. Again, a consistent experimental trend is correlated over a wide range of Gr. Both laminar and Rayleigh-Bénard correlations are shown, with the latter demonstrating a significant turbulent component to the correlation. The 95% confidence limit of the fitted Nu_s is ±3.3. The laminar correlation is consistent with the one used by the transient closed cavity model in Nicholas et al. [35]. The difference between the closed and open cavity correlations is attributed to the difference in the core slip. As discussed in Sections 5.1-5.5, the slip of the vortex structures in the open cavity was measured to be 12-16% and that in the closed cavity less than 1%, consistent with previous measurements [16, 17, 22]. The higher slip in the open cavity is caused by increased momentum exchange from the throughflow which reduces swirl in the core, increasing the velocity difference between the shroud boundary layer and the core, enhancing the heat transfer akin to forced convection. As such, an open cavity without cobs is likely to be governed by a higher magnitude of shroud heat transfer.

5.7 Plume Mass Flow Rate and Circumferential Pressure Gradient

As discussed in Section 4.2 and illustrated in Figure 3, Tang and Owen [36] derived a model for a closed rotating cavity based on plumes of fluid moving radially in the core, transferring (in an energy balance) heat from the hot shroud to the cold hub. A circumferential pressure gradient was assumed in the core, physically created by the cyclonic and anti-cyclonic vortex pairs. The non-dimensional mass flow rate of the plume, C_w, was proportional to the measured difference in pressure between the centres of the vortices, Δp, and the number of vortex pairs, n – see Equation 3. Here, C_w is correlated with Gr_s and the data is plotted in Figure 13 for both steady-state and transient conditions, for both the open and closed cavities. This type of correlation for the open cavity, and for transient conditions, is the first of its kind. Again, shroud temperature, speed and Rossby transients all feature in this data with a remarkably consistent correlation over a wide range of Gr, whether the flow is in a steady-state or transient condition. The 95% confidence limits of the fitted $\mathrm{nRe}_\phi C_{\Delta p}/2$ are $\pm 2.7 \times 10^4$ and $\pm 8.1 \times 10^3$ for the closed and open cavity correlations, respectively.

As with shroud heat transfer, different correlations were found for the open and closed cavities. In this case, for a given Gr_s the plume mass flow for the closed cavity is higher than that for the open cavity. This again can be explained by the difference in the core slip. The high slip in the open cavity results in lower effective buoyancy forces, suppressing the radial fluid movement. For the open cavity, the plume mass flow rate presents a maximum mass exchange between the cavity flow and the axial throughflow. Note again that transient data were only possible where stable, coherent structures existed in the cavity and the flow was dominated by buoyancy.

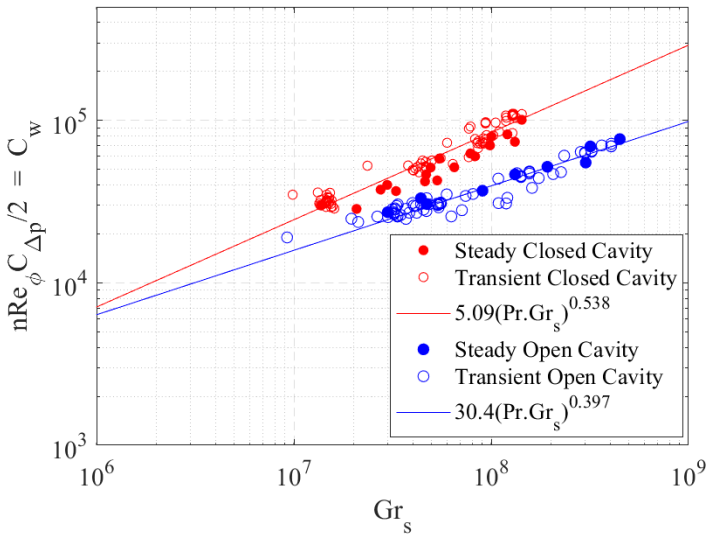

Figure 13: Experimental plume mass flow correlation for both open and closed cavities under steady and transient conditions.

6. CONCLUSIONS

For the first time, experiments and modelling have been used to investigate the flow and heat transfer in the rotating cavities in compressors under transient conditions. Here the physical phenomena are dominated by buoyancy effects created by rotation and temperature gradients. The unsteady rotating flow structure features pairs of cyclonic and anti-cyclonic vortices, separated from the rotor discs by laminar Ekman layers. A single pair of asymmetric vortices was always present in open cavities, with the cyclonic vortex the larger. The non-dimensional Rossby number (Ro) of the axial throughflow at the bore governs momentum and enthalpy exchange with the cavity and influences the slip of these structures relative to the disc; typically, the structures slipped at 10-15% relative to the rotor speed. In a closed cavity either three or four pairs of structures rotating at near solid-body rotation were detected, the number of pairs depending on the rotational Reynolds (Re_ϕ) and Grashof (Gr) numbers.

These flow structures were measured under transient conditions, where Gr, Re_ϕ and Ro were changed to simulate effects associated with aero-engine accelerations. The transient shroud heat transfer was directly linked to the flow structure in the cavity. The magnitude of the pressure differences in the vortex structures (driven by buoyant flow) was proportional to Gr and during the transient, they disappeared when the convective heat flux at the shroud approached zero. The slip relative to the disc and the number of vortex pairs was shown to change during transient conditions, suggesting a transitional Re_ϕ for the stability of these unsteady structures. Even in the steady state the measurements indicated small but persistent variation in slip associated with an aperiodic unsteadiness in the structures.

Pragmatic engine design methodology requires dimensional analysis and fluid-dynamically scaled correlations of heat transfer, usually in the form of power-law exponents. Here the shroud Nusselt number was correlated against Grashof number for both closed and open rotating cavities. Both steady-state and transient correlations were produced, the latter the first of their kind for compressor cavities. There was a remarkable agreement between the correlations across a wide range of Gr. The best-fit correlation in the open cavity was identical to the laminar flat-plate free convection correlation of $Nu_s = 0.54Ra_s^{0.25}$. Consistent correlations for the radial mass flow rate of hot and cold plumes against Gr were produced for both steady-state and transient conditions in both closed and open cavities; again, the latter is the first of its kind. From a practical perspective, the experimental data and validated modelling can be used to scale to the engine and inform thermo-mechanical design codes and methods.

ACKNOWLEDGEMENTS

This work was supported by the UK Engineering and Physical Sciences Research Council under the grant number EP/P003702/1 in collaboration with Rolls-Royce plc. The authors gratefully acknowledge the support of Carl Sangan, Oliver Pountney and, especially, the late Professor J Michael Owen.

APPENDIX: TRANSIENT EXPERIMENT PARAMETERS

Case	$\mathrm{Re}_\phi/10^6$	$\beta\Delta T$	$\mathrm{Gr}/10^{11}$	Ro	n
closed cavity shroud temperature transients					
A	0.81	0.16 → 0	1.0 → 0	n/a	3
B	1.6	0.14 → 0	3.4 → 0	n/a	3
C	2.3	0.14 → 0	7.4 → 0	n/a	3
D_1	2.9	0.12 → 0	10 → 0	n/a	4
D_2	2.9	0.12 → 0.08	10 → 6.0	n/a	4
closed cavity speed transients (accel. & decel.)					
E	0.81 – 1.6	0.16 – 0.12	1.1 – 2.9	n/a	3
F	0.81 – 2.3	0.16 – 0.12	1.1 – 6.5	n/a	3
G	0.80 – 2.7	0.16 – 0.12	1.1 – 8.7	n/a	3-4
H	0.80 – 2.9	0.16 – 0.13	1.1 – 10	n/a	4

Table 1: Summary of main parameters for investigated transient cases in the closed cavity configuration

Case	$\mathrm{Re}_\phi/10^6$	$\beta\Delta T$	$\mathrm{Gr}/10^{11}$	Ro	n
open cavity shroud temperature transients					
J_1	0.80	0.18→ 0	1.0→ 0	0.2	1
J_2	0.80	0.18→ 0.01	1.0→ 0.1	0.2	1
K_1	1.6	0.18→ 0	4.6→ 0	0.2	1
K_2	1.6	0.18→ 0.02	4.6→ 0.5	0.2	1
L_1	2.3	0.18→ 0	9.5→ 0	0.2	1
L_2	2.3	0.18→ 0.05	9.5→ 1.0	0.2	1
M	2.6	0.17→ 0.07	11→ 2.5	0.2	1
N_1	2.9	0.17→ 0	14→ 0	0.2	1
N_2	2.9	0.17→ 0.09	14→ 5.0	0.2	1
N_3	2.9	0.17→ 0	14 → 0	0.35	1
open cavity speed transients (accel. & decel.)					
O	0.81 – 1.6	0.18 – 0.12	1.3 – 2.9	0.2	1
P	0.81 – 2.3	0.18 – 0.13	1.3 – 6.8	0.2	1
R	0.81 – 2.6	0.17 – 0.15	1.2 – 10	0.2	1
S_1	0.81 – 2.9	0.17 – 0.14	1.2 – 11	0.2	1
S_2	0.81 – 2.9	0.17 – 0.18	1.2 – 15	0.2 – 0.05	1
S_3	0.81 – 2.9	0.17 – 0.11	1.2 – 9.3	0.2 – 0.33	1
open cavity Rossby transients					
T_1	0.80	0.18	1.0	0.2 – 0.4	1
T_2	0.80	0.18	1.0	0.2 – 1.0	1
U	1.6	0.18	4.6	0.2 – 0.4	1
W	2.3	0.17	8.9	0.2 – 0.4	1

Table 2: Summary of main parameters for investigated transient cases in the open cavity configuration

NOMENCLATURE

Roman letters

a	inner radius of cavity (hub) [m]
a'	radius of innermost thermocouple on disc diaphragm [m]
b	outer radius of cavity (shroud) [m]
b'	radius of outermost thermocouple on disc diaphragm [m]
f_d	rotational frequency of discs [Hz]
f_s	rotational frequency of the flow structure [Hz]
$f_{s,1}$	rotational frequency of one vortex pair [Hz]
G	cavity gap ratio
g	gravitational acceleration [m/s^2]
i	inner radius of constant-thickness disc diaphragm [m]
k	thermal conductivity [W/mK]
N	rotational speed of discs [rpm]
n	number of vortex pairs
o	outer radius of constant-thickness disc diaphragm [m]
p	static pressure [Pa]
$\bar{p}$	mean static pressure [Pa]
q	heat flux [W/m^2]
r	radius [m]
s	axial cavity width [m]
t	time [s]
T	temperature [K]
W	axial throughflow velocity [m/s]
x	non-dimensional radial location

Greek letters

α	thermal diffusivity [m^2/s]
β	volume expansion coefficient [K^{-1}]
γ	angular separation of unsteady pressure sensors [rad]
Θ	non-dimensional temperature ($= \frac{T-T_{d,a'}}{T_{d,b'}-T_{d,a'}}$)
μ	dynamic viscosity [m^2/s]
ν	momentum diffusivity [m^2/s]
ρ	density [kg/m^3]
χ	compressibility parameter ($= \frac{\mathrm{Ma}^2}{\beta\Delta T}$, where $\mathrm{Ma}^2 = \frac{\Omega^2 b^2}{\gamma R(T_b+T_a)/2}$)

ψ non-dimensional heat flux

Ω angular velocity of disc [rad/s]

Dimensionless groups

C_p pressure coefficient

$C_{\Delta p}$ pressure variation coefficient

C_w plume mass flow rate

Fo Fourier number

Gr Grashof number (= $\mathrm{Re}_\phi^2 \beta \Delta T$)

Gr_s shroud Grashof number (= $\frac{\rho_{c,b}^2 \Omega^2 b}{\mu^2} \left(\frac{s}{2}\right)^3 \beta \left(T_s - T_{c,b}\right)$)

Nu Nusselt number (= $\frac{qL}{k\Delta T}$)

Pr Prandtl number (= $\frac{\nu}{\alpha}$)

Ra Rayleigh number (= PrGr)

Re_ϕ rotational Reynolds number (= $\frac{\rho \Omega b^2}{\mu_f}$)

Ro Rossby number (= $\frac{W}{\Omega a}$)

$\beta \Delta T$ buoyancy parameter (= $\frac{T_b - T_a}{(T_b + T_a)/2}$)

Superscripts and subscripts

$a; a'; b; b'$ values at $r = a; r = a'; r = b; r = b'$

c value in the fluid core

d value on the disc surface

f value in the axial cooling flow

s shroud

ϕ,r,z circumferential, radial and axial direction

REFERENCES

[1] Diemel, E., Odenbach, S., Uffrecht, W., Villazon, J.R., Valencia, A.G. and Reinecke, M. "High Speed Single Cavity Rig With Axial Throughflow of Cooling Air: Rig Structure and Periphery." *ASME Paper GT2019-91265* (2019)DOI 10.1115/GT2019-91265.

[2] Atkins, N.R. "Investigation of a Radial-Inflow Bleed as a Potential for Compressor Clearance Control." *ASME Paper GT2013-95768* (2013)DOI 10.1115/GT2013-95768.

[3] Owen, J.M. and Long, C.A. "Review of Buoyancy-Induced Flow in Rotating Cavities." *ASME J. Turbomach.* Vol. 137 No. 11 (2015). DOI 10.1115/1.4031039.

[4] Tang, H. and Owen, J.M. "Theoretical Model of Buoyancy-Induced Heat Transfer in Closed Compressor Rotors." *ASME J. Eng. Gas Turbines Power* Vol. 140 No. 3 (2017). DOI 10.1115/1.4037926.

[5] Sun, Z., Kifoil, A., Chew, J.W. and Hills, N.J. "Numerical Simulation of Natural Convection in Stationary and Rotating Cavities." *ASME Paper GT2004-53528* (2004)DOI 10.1115/GT2004-53528.

[6] Bohn, D., Deuker, E., Emunds, R. and Gorzelitz, V. "Experimental and Theoretical Investigations of Heat Transfer in Closed Gas-Filled Rotating Annuli." *ASME J. Turbomach.* Vol. 117 No. 1 (1995): pp. 175–183. DOI 10.1115/1.2835635.

[7] King, M.P., Wilson, M. and Owen, J.M. "Rayleigh-Bénard Convection in Open and Closed Rotating Cavities." *ASME J. Eng. Gas Turbines Power* Vol. 129 No. 2 (2007): pp. 305–311. DOI 10.1115/1.2432898.

[8] Owen, J.M. "Thermodynamic Analysis of Buoyancy-Induced Flow in Rotating Cavities." *ASME J. Turbomach.* Vol. 132 No. 3 (2010). DOI 10.1115/1.2988170.

[9] Pitz, D.B., Marxen, O. and Chew, J.W. "Onset of convection induced by centrifugal buoyancy in a rotating cavity." *J. Fluid Mech.* Vol. 826 (2017): pp. 484–502. DOI 10.1017/jfm.2017.451.

[10] Pitz, D.B., Chew, J.W., Marxen, O. and Hills, N.J. "Direct Numerical Simulation of Rotating Cavity Flows Using a Spectral Element-Fourier Method." *ASME J. Eng. Gas Turbines Power* Vol. 139 No. 7 (2017). DOI 10.1115/1.4035593.

[11] Pitz, D.B., Chew, J.W. and Marxen, O. "Large-Eddy Simulation of Buoyancy-Induced Flow in a Sealed Rotating Cavity." *ASME J. Eng. Gas Turbines Power* Vol. 141 No. 2 (2018). DOI 10.1115/1.4041113.

[12] Gao, F., Pitz, D.B. and Chew, J.W. "Numerical investigation of buoyancy-induced flow in a sealed rapidly rotating disc cavity." *International Journal of Heat and Mass Transfer* Vol. 147 (2020): p. 118860. DOI 10.1016/j.ijheatmasstransfer.2019.118860.

[13] Pitz, D.B. and Wolf, W.R. "Coriolis force effects on radial convection in a cylindrical annulus." *International Journal of Heat and Mass Transfer* Vol. 189 (2022). DOI 10.1016/j.ijheatmasstransfer.2022.122650.

[14] Bohn, D., Dibelius, G.H., Deuker, E. and Emunds, R. "Flow Pattern and Heat Transfer in a Closed Rotating Annulus." *ASME J. Turbomach.* Vol. 116 No. 3 (1994): pp. 542–547. DOI 10.1115/1.2929443.

[15] Bohn, D., Emunds, R., Gorzelitz, V. and Krüger, U. "Experimental and Theoretical Investigations of Heat Transfer in Closed Gas-Filled Rotating Annuli II." *ASME J. Turbomach.* Vol. 118 No. 1 (1996): pp. 11–19. DOI 10.1115/1.2836590.

[16] Jackson, R.W., Tang, H., Scobie, J.A., Owen, J.M. and Lock, G.D. "Measurement of Heat Transfer and Flow Structures in a Closed Rotating Cavity." *ASME J. Eng. Gas Turbines Power* Vol. 144 No. 5 (2022). DOI 10.1115/1.4053392.

[17] Lock, G.D., Jackson, R.W., Pernak, M.J., Pountney, O.J., Sangan, C.M., Owen, J.M., Tang, H. and Scobie, J.A. "Stratified and Buoyancy-Induced Flow in Closed Compressor Rotors." *ASME J. Turbomach.* Vol. 145 No. 1 (2023). DOI 10.1115/1.4055448.

[18] Farthing, P.R., Long, C.A., Owen, J.M. and Pincombe, J.R. "Rotating Cavity With Axial Throughflow of Cooling Air: Flow Structure." *ASME J. Turbomach.* Vol. 114 No. 1 (1992): pp. 237–246. DOI 10.1115/1.2927991.

[19] Tian, S., Tao, Z., Ding, S. and Xu, G. "Investigation of Flow and Heat Transfer Instabilities in a Rotating Cavity With Axial Throughflow of Cooling Air." *ASME Paper GT2004-53525* (2004)DOI 10.1115/GT2004-53525.

[20] Bohn, D.E., Deutsch, G.N, Burkhard, S. and Burkhardt, C. "Flow Visualisation in a Rotating Cavity With Axial Throughflow." *ASME Paper 2000-GT-0280* (2000)DOI 10.1115/2000-GT-0280.

[21] Long, C.A., Miché, N.D.D. and Childs, P.R.N. "Flow measurements inside a heated multiple rotating cavity with axial throughflow." *International Journal of Heat and Fluid Flow* Vol. 28 No. 6 (2007): pp. 1391–1404. DOI 10.1016/j.ijheatfluidflow.2007.04.010.

[22] Jackson, R.W., Tang, H., Scobie, J.A., Pountney, O.J., Sangan, C.M., Owen, J.M. and Lock, G.D. "Unsteady Pressure Measurements in a Heated Rotating Cavity." *ASME J. Eng. Gas Turbines and Power* Vol. 144 No. 4 (2022). DOI 10.1115/1.4053390.

[23] Gao, F. and Chew, J.W. "Flow and Heat Transfer Mechanisms in a Rotating Compressor Cavity Under Centrifugal Buoyancy-Driven Convection." *ASME J. Eng. Gas Turbines Power* Vol. 144 No. 5 (2022): p. 051010. DOI 10.1115/1.4052649.

[24] Gao, F. and Chew, J.W. "Ekman Layer Scrubbing and Shroud Heat Transfer in Centrifugal Buoyancy-Driven Convection." *ASME J. Eng. Gas Turbines Power* Vol. 143 No. 7 (2021). DOI 10.1115/1.4050366.

[25] Bohn, D. and Gier, J. "The Effect of Turbulence on the Heat Transfer in Closed Gas-Filled Rotating Annuli for Different Rayleigh Numbers." *ASME Paper 98-GT-542* (1998)DOI 10.1115/98-GT-542.

[26] Saini, D. and Sandberg, R.D. "Simulations of compressibility effects in centrifugal buoyancy-induced flow in a closed rotating cavity." *International Journal of Heat and Fluid Flow* Vol. 85 (2020): p. 108656. DOI 10.1016/j.ijheatfluidflow.2020.108656.

[27] Gao, F., Pitz, D.B. and Chew, J.W. "Numerical investigation of buoyancy-induced flow in a sealed rapidly rotating disc cavity." *International Journal of Heat and Mass Transfer* (2019)DOI 10.1016/j.ijheatmasstransfer.2019.118860.

[28] Long, C.A. and Childs, P.R.N. "Shroud heat transfer measurements inside a heated multiple rotating cavity with axial throughflow." *International Journal of Heat and Fluid Flow* Vol. 28 No. 6 (2007): pp. 1405–1417. DOI 10.1016/j.ijheatfluidflow.2007.04.009.

[29] Tang, H. and Owen, J.M. "Effect of Buoyancy-Induced Rotating Flow on Temperatures of Compressor Disks." *ASME J. Eng. Gas Turbines Power* Vol. 139 No. 6 (2017). DOI 10.1115/1.4035400.

[30] Jackson, R.W., Tang, H., Scobie, J.A., Pountney, O.J., Sangan, C.M., Owen, J.M. and Lock, G.D. "Analysis of Shroud and Disk Heat Transfer in Aero-Engine Compressor Rotors." *ASME J. Eng. Gas Turbines Power* Vol. 143 No. 9 (2021). DOI 10.1115/1.4050631.

[31] Rozman, M., DeShong, E.T., Berdanier, R.A., Thole, K.A. and Robak, C. "Characterizing Flow Instabilities During Transient Events in the Turbine Rim Seal Cavity." *ASME J. Turbomach.* Vol. 145 No. 3 (2023): p. 031014. DOI 10.1115/1.4055748.

[32] Burkhardt, C. and Mayer, A. "Transient Thermal Behaviour of a Compressor Rotor With Axial Cooling Air Flow and Co-Rotating or Contra-Rotating Shaft." *AGARD CP527*: pp. 21.1–21.9. 1992.

[33] Luberti, D., Patinios, M., Jackson, R.W., Tang, H., Pountney, O.J., Scobie, J.A., Sangan, C.M., Owen, J.M. and Lock, G.D. "Design

and Testing of a Rig to Investigate Buoyancy-Induced Heat Transfer in Aero-Engine Compressor Rotors." *ASME J. Eng. Gas Turbines Power* Vol. 143 No. 4 (2021). DOI 10.1115/1.4048601.

[34] Pountney, O.J., Patinios, M., Tang, H., Luberti, D., Sangan, C.M., Scobie, J.A., Owen, J.M. and Lock, G.D. "Calibration of thermopile heat flux gauges using a physically-based equation." *Proceedings of the Institution of Mechanical Engineers, Part A: Journal of Power and Energy* Vol. 235 No. 7 (2021): pp. 1806–1816. DOI 10.1177/0957650920982103.

[35] Nicholas, T.E.W., Pernak, M.J., Scobie, J.A., Lock, G.D. and Tang, H. "Transient Heat Transfer and Temperatures in Closed Compressor Rotors." *Appl. Therm. Eng., submitted* (2023)DOI 10.2139/ssrn.4333657.

[36] Tang, H. and Owen, J.M. "Plume Model for Buoyancy-Induced Flow and Heat Transfer in Closed Rotating Cavities." *ASME J. Turbomach.* Vol. 145 No. 1 (2022). DOI 10.1115/1.4055449.

[37] Tang, H., Shardlow, T. and Owen, J.M. "Use of Fin Equation to Calculate Nusselt Numbers for Rotating Disks." *ASME J. Turbomach.* Vol. 137 No. 12 (2015). DOI 10.1115/1.4031355.

[38] Tang, H. and Owen, J.M. "Effect of Radiation on Heat Transfer Inside Aeroengine Compressor Rotors." *ASME J. Turbomach.* Vol. 143 No. 5 (2021). DOI 10.1115/1.4050114.